Water Resources Research

RESEARCH ARTICLE
10.1029/2018WR024542

Special Section:
Advances in remote sensing, measurement, and simulation of seasonal snow

Snowmelt Detection with Calibrated, Enhanced-Resolution Brightness Temperatures (CETB) in Colorado Watersheds

Mitchell T. Johnson[1,2], Joan Ramage[3], Tara J. Troy[1,4], and Mary J. Brodzik[5]

[1]Department of Civil and Environmental Engineering, Lehigh University, Bethlehem, PA, [2]Science and Technology Corporation, Hampton, VA, [3]Department of Earth and Environmental Sciences, Lehigh University, Bethlehem, PA, [4]Department of Civil Engineering, University of Victoria, Victoria, BC, Canada, [5]University of Colorado, NSIDC/CIRES, Boulder, CO

Abstract Understanding the timing of snowmelt is critical for water resources management in snow-dominated watersheds. Passive microwave remote sensing can be used to estimate snowmelt events through brightness temperature satellite observations. Previous studies were limited to lower resolution (~25 km or coarser) datasets, making it difficult to quantify snowpack variability in heterogeneous, high-relief areas. This study investigates the use of recently available Calibrated, Enhanced-Resolution Passive Microwave Daily EASE-Grid 2.0 Brightness Temperature ESDR (CETB) to estimate snowmelt timing at much higher spatial resolution (~3-6 km) than has been previously available. This study investigates the effectiveness of the CETB product for snowmelt detection in several locations in Colorado (North Park, Rabbit Ears, Fraser) that were the sites of previous ground/airborne surveys during the NASA Cold Land Processes Field Experiment (CLPX 2002-2003), along with data for the Senator Beck Basin from the Center for Snow and Avalanche Studies (CSAS). We compare melt variability with nearby air temperature and stream discharge to show that the new CETB product allows detection of hydrologic processes in mountainous watersheds. We show that the higher resolution CETB product can detect snowmelt in heterogeneous terrain more accurately than the coarser resolution product in terms of the number of winter melt events and seasonal melt onset date. This work lays the foundation for the utilization of higher resolution reprocessed CETB data for snowpack evolution more broadly in a range of environments.

Key Points:
- CETB datasets can detect snowmelt in a heterogeneous mid-latitude environment using Diurnal Amplitude Variation (DAV) method
- CETB signal in 36/37 GHz datasets detects hydrologic processes
- Higher resolution CETB datasets can resolve the spatial variability of landscape more accurately than legacy coarser resolution products

Supporting Information:
- Supporting Information S1

Correspondence to:
M. T. Johnson,
mij216@lehigh.edu

Citation:
Johnson, M. T., Ramage, J., Troy, T. J., & Brodzik, M. J. (2020). Snowmelt Detection with Calibrated, Enhanced-Resolution Brightness Temperatures (CETB) in Colorado Watersheds. *Water Resources Research*, *56*, e2018WR024542. https://doi.org/10.1029/2018WR024542

Received 1 DEC 2018
Accepted 2 JAN 2020
Accepted article online 05 JAN 2020

1. Introduction

Quantifying snowmelt timing is critical for water resources management in many mountainous watersheds, as they receive the majority of their precipitation as winter and spring snow (Serreze et al., 1999). Peak stream discharge often coincides with the snowmelt season in such basins, and studies have shown that a warming climate would likely cause earlier seasonal snowmelt and an earlier shift in snowmelt-driven streamflow globally (Barnett et al., 2005; Stewart, 2009). The western US is of particular interest, since earlier shifts in snowmelt-derived streamflow have been observed since the mid-20th century (McCabe & Clark, 2005; Regonda et al., 2005; Stewart et al., 2004). Changes in climate, land cover, and population growth in the western United States create a need for more information related to mountain hydrology (Bales et al., 2006). In addition to the main melt onset timing crucial for spring runoff determination, it is also important to have an understanding of winter melting events (Semmens et al., 2013), especially in mid-latitude environments prone to snowpack variations that influence the snow stratigraphy and underlying soil layers (Tuttle & Jacobs, 2019). Satellite-based snowmelt products may decrease the reliance on ground measurements, which cannot capture the spatial and temporal variability of snowpack properties in high-relief and heterogeneous terrain.

Seasonal snowmelt, defined here as the period in which snowmelt leads to the disappearance of the snowpack, begins with diurnal cycles of daytime melting and overnight refreeze. Isolated early melt events also occur during winter at mid-latitudes that precede seasonal snowmelt (Tuttle & Jacobs, 2019). Passive microwave radiometers have been used to detect a melting snowpack due to the difference in physical properties of wet and dry snow (Burke et al., 1984). Radiometers retrieve the passive microwave signal through a derived

measurement called brightness temperature. The brightness temperature may be approximated as a function of the emissivity and the land surface temperature: $T_B \sim \varepsilon T_s$, where T_B is brightness temperature, ε is emissivity, and T_s is surface temperature (Chang et al., 1976). The emissivity changes significantly between a frozen, dry snowpack and a liquid water-containing snowpack (Mätzler, 1987). Therefore, sub-daily measurements of brightness temperature capture the large variation between the morning and evening overpasses associated with diurnal cycles of melt and refreeze (Foster et al., 1984).

Passive microwave brightness temperature products have been derived from sensors that include the Scanning Multi-channel Microwave Radiometer (SMMR) from 1978 to 1987, the Advanced Microwave Scanning Radiometer for EOS (AMSR-E) from 2002 to 2011, and Special Sensor Microwave/Imager (SSM/I) and Special Sensor Microwave Imager/Sounder (SSMIS) instruments from 1987 to present. Temporal subsets of these products were historically available at a coarse spatial resolution (~25 km), but gridding methods were not consistent for all sensors, and input swath data from the SSM/I-SSMIS sensor series were not cross-calibrated. To perform legitimate climate record studies for the complete observation record, the remote sensing community needed a systematically-gridded brightness temperature product. To address this need, Brodzik et al. (2018) developed the Calibrated, Enhanced-Resolution Brightness Temperature (CETB) product, which spans the entire available passive microwave record for SMMR, AMSR-E and the SSM/I-SSMIS sensors and uses newly available cross-calibration records for SSM/I-SSMIS (Sapiano et al., 2013). The CETB product includes traditional 25 km images and enhanced-resolution images derived using the radiometer version of the Scatterometer Image Reconstruction (rSIR) method, with spatial resolutions up to 3.125 km for the highest-frequency channels (Long & Brodzik, 2016). Using CETB low-resolution (25 km) and enhanced-resolution (up to 3.125 km) data, we assessed the accuracy of these datasets for snowmelt detection in heterogeneous, mid-latitude settings, focusing on the vertically polarized channels at 36.5 GHz for AMSR-E and 37 GHz for SSM/I onboard the Defense Meteorological Satellite Program F-13 satellite.

The absolute value of the difference in brightness temperature between the morning and the evening overpasses is called the diurnal amplitude variation (DAV). The DAV method for snowmelt detection was originally developed with coarser resolution, heritage passive microwave products in a glaciated environment (Ramage & Isacks, 2002). Higher emissivity from liquid water near the snow surface rapidly increases the observed passive microwave brightness temperature. Subsequent refreezing causes the brightness temperature to drop below the previous cold, dry state due to enhanced scattering from grain metamorphism. Thus, the DAV magnitude increases, due to the diurnal freeze/thaw cycling. DAV is smaller during both the coldest winter months and snow-off periods than during melt events. Furthermore, DAV continues to increase with more cycles of melt-refreeze, due to continued snowpack metamorphism. Melt and freeze cycles cause snow grain size to increase, which further attenuates the passive microwave signal, causing much lower T_B values for a refrozen snowpack as opposed to a dry winter snowpack that has never melted (Burke et al., 1984). Algorithms have been developed to estimate the melt onset date (MOD) and end of high DAV by counting the number of instances where the DAV and T_B exceed specified thresholds in a given time window (Monahan & Ramage, 2010). Studies have also shown that increased stream discharge either coincides with or directly follows the end of the high DAV period in snow-dominated watersheds (Kopczynski et al., 2008; Ramage et al., 2006; Vuyovich & Jacobs, 2011). Other studies have used passive microwave DAV methods for snowmelt detection in Arctic and Antarctic settings (Tedesco, 2007; Tedesco et al., 2007, 2009), and there has been some work with passive microwaves and snowmelt detection in mid-latitude environments with seasonal snow cover, such as the Sierra Nevada Mountains, CA (Li et al., 2012). Semmens et al. (2014) showed a high DAV signal corresponding with the melt season at Senator Beck Basin, CO, and Tuttle and Jacobs (2019) recently used AMSR-E data to further examine snowmelt in that basin. Additionally, previous work has successfully used the DAV method for detection of early melt events (EMEs) in the Yukon River Basin, defined as shorter duration melt events that precede the seasonal MOD (Semmens et al., 2013). These events are important because they cause ice layers in the snowpack and can impact the performance of microwave-based SWE algorithms (Foster et al., 1984). Our study is one of the first to employ the CETB datasets for snowmelt detection in a mid-latitude environment (~37-40° N).

Our study seeks to answer the following questions: 1) Can the DAV method for snowmelt detection be used with the CETB products in a mid-latitude mountainous environment?; 2) What are the T_B and DAV thresholds necessary for optimal algorithm performance in detecting melt events and melt onset date?; and 3) Can

the enhanced-resolution CETB product better resolve spatial differences given its enhanced spatial resolution? To address these questions, we use the CETB product at four mountainous sites in Colorado with extensive ground observations, allowing us to refine snowmelt algorithms and detection of spatial variability with ground validation of melt days.

2. Data

Three main sources of data were used in this study: the Calibrated, Enhanced-Resolution Brightness Temperature (CETB) product (Brodzik et al., 2018), ground observations taken during the NASA Cold Land Processes Experiment (CLPX) (Elder & Goodbody, 2004), and ground observations at Senator Beck Basin from the Center for Snow and Avalanche Studies (CSAS) (Landry et al., 2014). Additionally, we used the 1/3 arc-second National Elevation Dataset (NED) to calculate the average elevations of each pixel (USGS, 2013). The study areas in Colorado, USA are shown in Figure 1.

2.1. Calibrated, Enhanced-Resolution Brightness Temperature (CETB)

We used the Calibrated, Enhanced-resolution Passive Microwave Daily EASE-Grid 2.0 Brightness Temperature (CETB) Earth System Data Record product (Brodzik et al., 2018) obtained from the National Snow and Ice Data Center (NSIDC) Distributed Active Archive Center (DAAC). This dataset was generated from calibrated swath brightness temperature (T_B) data for the complete data records from SMMR, SSM/I-SSMIS and AMSR-E. The product includes enhanced-resolution rSIR images up to 3.125 km, as well as relatively smooth, averaged images at the legacy 25 km spatial resolution. The CETB 25 km gridding procedure is a simple, "drop-in-the-bucket" average (GRD). For the GRD algorithm, the center of each swath measurement is mapped to a 25 km EASE-Grid cell. All measurements in a given time period in a given grid cell are averaged to produce a T_B value for that pixel. The rSIR algorithm is a computationally efficient, iterative image reconstruction method that is tuned to enhance spatial resolution (Long & Brodzik, 2016). The rSIR method uses all measurements whose effective field of view overlaps a given grid cell, weighted by the antenna measurement response function. For the remainder of this document, "GRD" will refer to the 25 km T_B data, while "rSIR" will refer to the enhanced resolution 3.125 km T_B data.

The CETB data includes twice-daily T_B images derived from measurements at approximately the same local time each day, within one hour variation at the latitudes studied. For AMSR-E at Colorado latitudes, morning overpass times occur between 08:30-09:30 UTC, and evening overpasses occur between 19:30-20:30 UTC. These overpass times equate to about 01:30 to 03:30 local time for morning overpasses and 12:30 to 14:30 local time for "evening" overpasses (dependent on daylight savings time). The SSM/I sensor onboard the Defense Meteorological Satellite Program F-13 satellite also provides twice-daily T_B measurements. Morning overpasses are approximately 07:30 to 09:30, while evening overpasses are 18:30 to 20:30 local time. We used the AMSR-E 36.5 GHz and DMSP-F13 37 GHz vertically polarized (36V and 37V, respectively) channels since they have been shown to be most sensitive to liquid water near the surface of the snowpack and therefore sensitive to melt and refreeze (Stiles, 1980). We used the 36V data derived from AMSR-E sensor onboard Aqua satellite, which was operational from 2002-2011, and 37V SSM/I data from the F-13 satellite for 2002-2009, which overlapped with ground measurements used in the study.

Due to the polar orbit pattern of the satellites, the CETB data contain missing values on some days at mid and lower latitudes, with the frequency of missed retrievals increasing with proximity to the equator. The frequency of missed retrievals is also a function of sensor swath width. For example, a one-year diurnal time series for a pixel at 40° N contains about 155 missing values out of 730; our sites have 155-200 missing values per year for AMSR-E, with a swath width of 1445 km. By comparison, the SSM/I sensor has a narrower swath width of 1400 km and produces a higher number of missed measurements, with 215-270 missed measurements per year at this latitude.

2.2. NASA Cold Land Processes Field Experiment (CLPX) Surface Observations

CLPX was undertaken in 2001-2003 to increase understanding of the terrestrial cryosphere, so that local-scale assessments of water fluxes, storage, and transformations could be extended to the regional and global scale. During the field campaign, an array of airborne and ground measurements were collected at multiple sites in the central Rocky Mountains of Colorado (Elder et al., 2009). All datasets produced are publicly available from the NSIDC DAAC. The CLPX study area was divided into three 25 km by 25 km meso-scale study

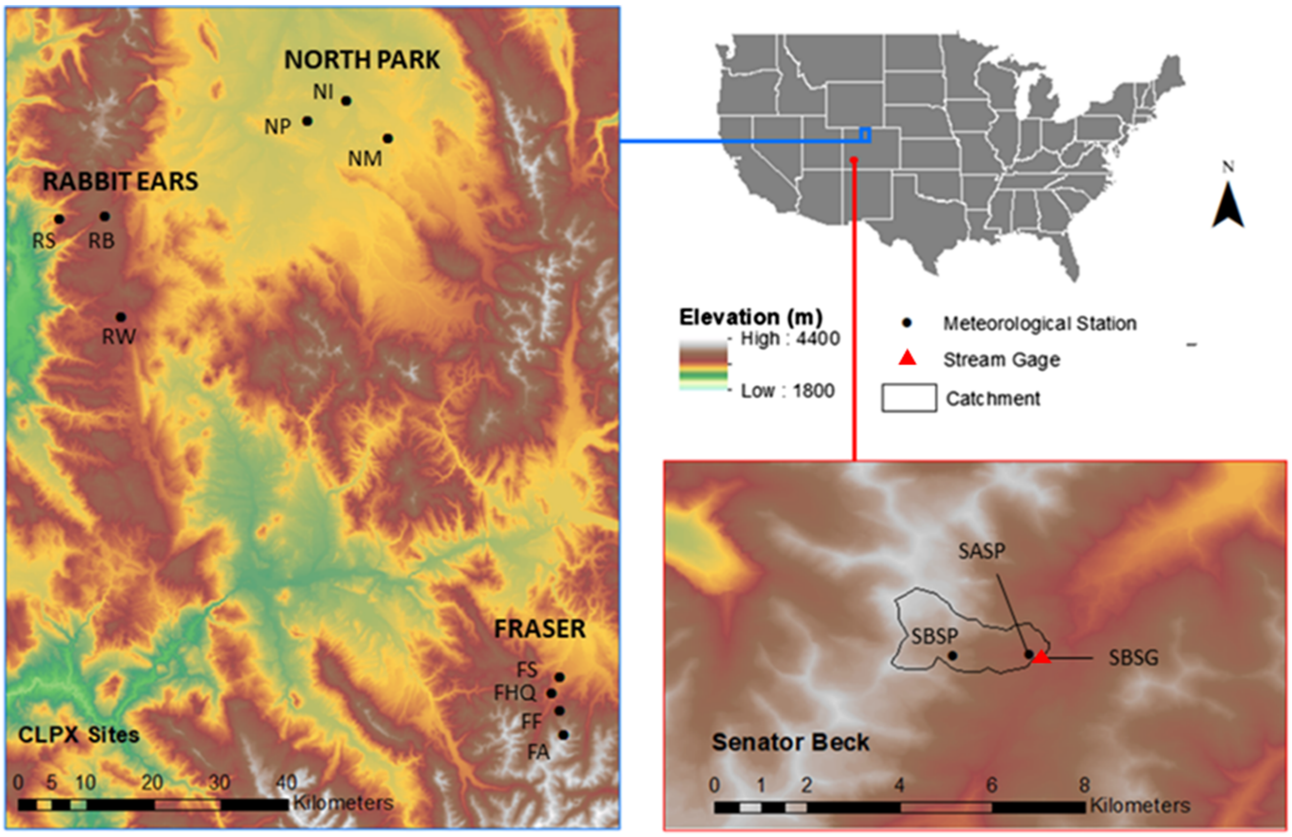

Figure 1. Regional overview of study areas with the elevation from the USGS 1/3 arc-sec DEM (USGS, 2013). Site IDs are listed as acronyms; See Table S1 of Supporting Information for full site names. Meteorological stations are shown as circles and the stream gage is represented with a triangle.

areas (MSAs): Fraser, Rabbit Ears, and North Park. Each MSA included varying elevation, land cover, and topographic complexity, and each MSA contained three nested 1-km by 1-km intensive study areas (ISAs) with a "main" meteorological station near the center of each ISA. The Fraser MSA included an additional meteorological station at the headquarters of the US Forest Service Fraser Experimental Forest, resulting in data from ten CLPX sites used in our study. The study locations are shown in Figure 1.

Our study relied on the "ISA Main Meteorological" datasets which provide an array of meteorological measurements in 10-minute intervals from September 2002 to September 2003 (Elder & Goodbody, 2004). Snowmelt validation was performed with sub-hourly measurements of both air temperature and snow depth, which were collected with a Vaisala HMP45C Temperature and Relative Humidity Probe and a Judd Ultrasonic Depth Sensor, respectively.

The Fraser MSA is the highest elevation and highest-relief of the three CLPX MSAs. See Table S1 of Supporting Information for a complete list of CLPX sites with geographic coordinates, station elevations, and average pixel elevations. Elevations range from 2500 m to over 3900 m, with moderate to deep snowpacks (up to 2 m at peak snowpack). Land cover is predominantly subalpine coniferous forest, with alpine tundra at the higher elevations. North Park is the lowest elevation and lowest relief. The MSA ranges from about 2400 m to 2700 m elevation and consists of grasslands, shrubs, and wetlands, and is typical of a prairie/tundra physiographic regime. This MSA contains the shallowest and most windswept snowpack due to its low elevation and location in a precipitation shadow. During 2003, the January 1 – March 31 average snowpack was less than 5 cm across North Park (Elder et al., 2009), and snow-free conditions in midwinter were common. Due to these characteristics, we excluded North Park sites from the threshold determination analysis since it was difficult to discern real melt events. Rabbit Ears is moderate elevation and moderate relief, ranging from about 2000 m to 3300 m, but it contains the most diverse land cover. Mixed deciduous/coniferous forest along with broad open meadows are found throughout the MSA. Orographic

precipitation in the higher elevation areas will develop some of the deepest snowpacks in Colorado (over 3 m in some areas at peak snowpack) (Cline et al., 2001).

2.3. Senator Beck Basin

The Center for Snow and Avalanche Studies (CSAS) operates and distributes ground data at the Senator Beck Basin, CO (Landry et al., 2014). These data are publicly available on the CSAS website. This basin is located in the San Juan Mountains in southwestern Colorado. We used data from two meteorological/snow stations: the Senator Beck Study Plot (SBSP) and the Swamp Angel Study Plot (SASP). Both of these sites are located in a small (~2.9 km^2) catchment with a stream gage at the outlet at 3362 m elevation (Figure 1). The stream that drains this catchment is an unnamed stream that ultimately feeds into Red Mountain Creek. We obtained the stream discharge data of this unnamed stream to compare with CETB and meteorological data. SBSP is located near the center of the catchment at an elevation of 3714 m, and SASP is located at 3371 m elevation near the catchment stream gage. SBSP is located above treeline in an alpine tundra environment in an exposed area that often experiences high winds (occasionally above 40 m/s). SASP is in a sheltered area at lower elevation and surrounded by sub-alpine forest. Therefore, it experiences lower winds and is better suited for measuring precipitation.

Both sites provide hourly data points of snow depth and air temperature from 2003-2017, and the stream gage data is available from 2005-2017. Snow depth was measured with a Campbell Scientific™ SR50 ultrasonic depth sounder, and temperature with a Campbell Scientific™ CS500 temperature and humidity sensor. The stream gage employs with a broad-crested, notched weir with a design capacity of about 40 (ft^3/s) and stage height is measured with Druck™ PDCR 1830-8388 transducer. Streamflow is then calculated from the stage height for late winter through summer. Streamflow is negligible during mid-winter since the stream is almost entirely fed by snowmelt. Data underwent a preliminary quality check by CSAS and are available for public download on the CSAS website.

3. Methods

The CETB data were compared with ground observations of air temperature, snow depth, snow melt, and stream discharge taken during the NASA Cold Land Processes Field Experiment (CLPX) and concurrent ground observations from CSAS at the Senator Beck Basin. We tested the accuracy of melt event detection, defined as a day with a decrease in snow depth and air temperature exceeding 0°C, and we tested the use of CETB data in a seasonal melt onset date (MOD) algorithm. The passive microwave sensors detect changes in wetness in the top layer of the snowpack; therefore, using snow wetness data would be the most direct comparison for what the CETB dataset perceives as a "melt" event and what in situ data detect as a melt event. However, time series of surface snow wetness data are largely unavailable. Decreasing SWE can be due to sublimation or to melt events that release water from the snowpack. Decreasing SWE coupled with above freezing air temperatures increases the likelihood that melt is occurring (without precluding sublimation).

A daily time series of SWE is not available at the CLPX sites to compare directly with the satellite dataset overpass times. However, a comparison of a nearby SNOTEL site (USDA NRCS, 2019) with daily SWE and snow depth measurements (Figure S1) demonstrated that the detected melt events using our definition of melt (air temperature above freezing accompanied by decreasing snow depth) agrees with SNOTEL melt events (air temperature above freezing accompanied by decreasing SWE). This comparison demonstrates the feasibility of using this definition of an observed melt event. Furthermore, other studies have used air temperature as a proxy for melt detection or shown that melt events correspond with air temperature above 0°C (Sturdivant et al., 2019; Tuttle & Jacobs, 2019).

In past studies, snowmelt was detected when both T_B and DAV thresholds were exceeded in a given day (Foster et al., 2011; Ramage & Isacks, 2002; Semmens et al., 2014). Both thresholds being exceeded indicates that the snowpack was dry and frozen (or refrozen) overnight, and daytime warming introduced liquid water in the near-surface of the snowpack. The earliest occurrences of high DAV tend to indicate surface melt that is then refrozen in the snowpack, and correspond with small or no discharge increase. The end of the high DAV cycles is coincident with or shortly before significant increases in melt generated runoff (timing varies by basin and depends on basin size and characteristics relative to the gauge location) and therefore are close to a hydrologist's definition of melt onset. The relationship is shown in detail for a small, gauged sub-arctic

basin in Ramage et al. (2006). Optimal T_B and DAV thresholds can vary with region and microwave sensor (Apgar et al., 2007; Li et al., 2012); we are testing whether they vary from previous studies with the new CETB product. We used a combination of two techniques for identifying thresholds in the Colorado region: we constructed histograms of T_B to separate different physical processes and used an optimization technique to maximize true positive and true negative melt events.

We constructed histograms of T_B for the available overlapping AMSR-E and SSM/I data (2003-2008) to examine the distribution. Ramage and Isacks (2002) used this technique in glaciated areas, which produced a bimodal distribution with the lower brightness temperature peak representing a frozen snowpack and the higher temperature peak representing a wet snowpack. The minimum between the peaks is an indication of the likely threshold, due to the large change in emissivity and change in T_B when a snowpack transitions between frozen and wet. We employed this technique for our sites of interest to estimate typical range of T_B values of melting and frozen snowpacks in Colorado, which allowed us to determine T_B thresholds for the region.

3.1. Winter Melt Event Detection – Error Statistics

In addition to histograms of T_B, the optimal combination of T_B and DAV thresholds was determined using observed snow data in combination with the remote sensing data to detect observed melt events with a binary classification technique. An observed melt event was defined as a day with a decrease in observed snow depth and an average air temperature greater than 0°C during the evening satellite overpass. We acknowledge that our observed melt criteria could be strengthened with additional in-situ datasets, like a time series of surface snow wetness, but such data are not widely available. Since the 36-37V channel is most sensitive to surface snowmelt, we assume an air temperature above 0°C with a decrease in snow depth would introduce some wetness into the surface of the snowpack. Therefore, when optimizing for AMSR-E, a melt event was flagged when the snow depth decreased and the average air temperature exceeded 0°C during 13:30 to 15:30 local time, while a melt event for SSM/I was flagged when the average air temperature exceeded 0°C for 18:00 to 20:00 local time. A true positive (TP) event is when melt is detected by the algorithm and also observed by meteorological station data. The rate of true positive (R_{TP}) is the number of true positive events divided by the number of total observed melt events, and is reported as a percentage. A true negative (TN) event is when melt is not detected by the algorithm and also not observed by meteorological station data. The rate of true negative (R_{TN}) is the number of true negative events divided by the total number of events with no melt observed. The error statistics were calculated for each combination of T_B and DAV thresholds, allowing T_B to vary between 240 and 270 K and DAV to vary between 8 and 30 K. The objective function maximizes the R_{TP} and R_{TN}. By definition, this also minimized the false positive (FP, type I error) and the false negative (FN, type II error). Our first objective was to find optimal thresholds for the detection of early season melt events. For optimization of the thresholds, we tested both DAV and T_B threshold ranges for January 1 to the date of peak snowpack at each site. We exclude days with missing data for optimization of melt thresholds. The optimization was conducted using four of the CLPX sites (FA, FS, RW, RB), and validation with the remaining three CLPX sites (FHQ, FF, RS). This optimization and validation with these selected sites was conducted separately at both rSIR and GRD resolutions. This means that different sets of thresholds could be determined for each data resolution.

3.2. Melt Onset Date Analysis

We used a variation of the algorithm developed by Monahan and Ramage (2010) to estimate the melt onset date (MOD) at each of the sites. We estimated MOD by identifying the first day of the year where both T_B and DAV thresholds are exceeded 5 times in a 7 day window. Previous studies used 3 out of 5 exceedances to indicate the MOD in the higher latitude Yukon Territory watershed, which had fewer early season melt events and a more clear seasonal snowpack ablation period (Apgar et al., 2007). This MOD definition often captured earlier ablation periods that were succeeded by significant periods of accumulation; therefore, we extended the window to 5 out of 7 days.

4. Results

To compare the spatial patterns produced by the rSIR and GRD resolutions, a warm winter day was chosen. Meteorological station data at the Fraser St. Louis Creek (FS) and Fool Creek (FF) sites indicated that air

temperatures exceeded freezing on February 14, 2003 and snowmelt was observed. Therefore, we would expect a snowmelt signal in microwave data. Figure 2 shows the CETB data for the evening overpass on February 14, 2003. This figure illustrates the spatial variability in the microwave signal due to the complex topography in the area, and the spatial differences between the CETB products at the two resolutions.

There is a clear difference in the details resolved by the rSIR data for both AMSR-E and SSM/I. The AMSR-E sensor more clearly indicates early melt and topographic variations which is likely due to its average overpass time that is closer to the average daytime high temperature. On February 14, 2003, the evening overpass was 247 K for Fraser Alpine (FA) and 250 K for FF (3100 m), while it was 254 K for Fraser Headquarters (FHQ) and 255 K for FS with the AMSR-E rSIR data. Meteorological station data showed that the air temperature exceeded freezing for FHQ and FS on this day, while other sites remained below freezing. The bottom two subplots show AMSR-E data for the same area on the same day. AMSR-E data for the GRD pixel containing FA, FF, and FHQ showed a T_B value of 246 K, with 258 K observed for the GRD pixel containing FS. SSM/I data showed a smaller range of T_B and a lower T_B values in the upper 240s K for the Fraser sites. It is important to note that the average overpass time for the SSM/I sensor is later in the day (~19:00 local time), when refreeze is possible. This could yield a smaller range of T_B values since more overpasses are likely to experience frozen conditions.

We compared the overall brightness temperature temporal distribution for each site, for both resolutions and sensors. Figure 3 shows the histograms of T_B for CLPX and Senator Beck sites with bins of 2 K. The histograms include data from AMSR-E and SSM/I for the calendar year 2003, for which CLPX data coincides for the 2003 melt season. Fraser and Rabbit Ears ground stations are each located within two adjacent GRD pixels, and their respective GRD histograms (dotted blue lines) include data from both of those pixels. The rSIR histograms (solid red lines) contain T_B data from each of the rSIR pixels in the respective MSA. Both Senator Beck stations are located in the same GRD pixel. The T_B histograms indicate a possible mixed distribution, potentially due to the heterogeneous terrain. It has been shown that low frequency T_B values between the main T_B populations tend to correspond with melt thresholds due to the significant emissivity change between frozen and wet snowpacks (Ramage & Isacks, 2002). A specific melt threshold for each site is unclear from the histograms, since minimum frequency values range from 245 K to 270 K.

4.1. Error Statistic Analysis for Threshold Determination

As discussed in the Methods, we used a binary classification technique. We detected melt and non-melt days to find the optimal T_B and DAV thresholds and then validated thresholds with ground data from meteorological stations. Using this method, the optimal thresholds at these sites for the AMSR-E sensor are T_B=249 K and DAV=13 K for rSIR, and optimal thresholds are TB=243K and DAV=14K for GRD. The optimal thresholds for SSM/I are T_B=247 K and DAV=10 K for both rSIR and GRD. The optimization was conducted over four of the CLPX sites (FA, FS, RW, RB), and the validation was conducted at the remaining three sites (FF, FHQ, RS). We conducted the analysis over a defined melt period of January 1 to the date of peak snowpack as recorded by each meteorological station. The January 1 to peak snowpack period was the most accurate because it allowed us to more effectively evaluate early season melt events. We found that late season melt events were more difficult to detect with the DAV method, since a saturated snowpack with continuous overnight melting will not have high amplitude variations, and thus will not trigger DAV thresholds.

For the calibration sites, the optimal thresholds with rSIR yielded true positive (R_{TP}) rates of 86% and 90% with AMSR-E and SSM/I, respectively (Table 1). Optimal GRD thresholds yielded true negative (R_{TN}) rates were 75% and 89% with AMSR-E and SSM/I, respectively. Validation with rSIR at other sites yielded true positive (R_{TP}) rates of 78% and 83% with AMSR-E and SSM/I, respectively. Validation of GRD thresholds yielded true positive rates of 46% and 65% with AMSR-E and SSM/I, respectively (Table 2). The true negative rates for GRD improved at the validation sites, likely because the algorithm was biased towards less melt detection and therefore is more likely to correctly estimate those days without melt. The rSIR data performed better in terms of true positive detection rates for the AMSR-E sensor and similarly to the GRD for the SSM/I sensor. See Tables 1 and 2 for a full list of error statistics for optimization and validation.

We also calculated error statistics for each individual CLPX site using the above optimized T_B and DAV thresholds. We calculated error statistics at each individual site for the above selected thresholds, so that

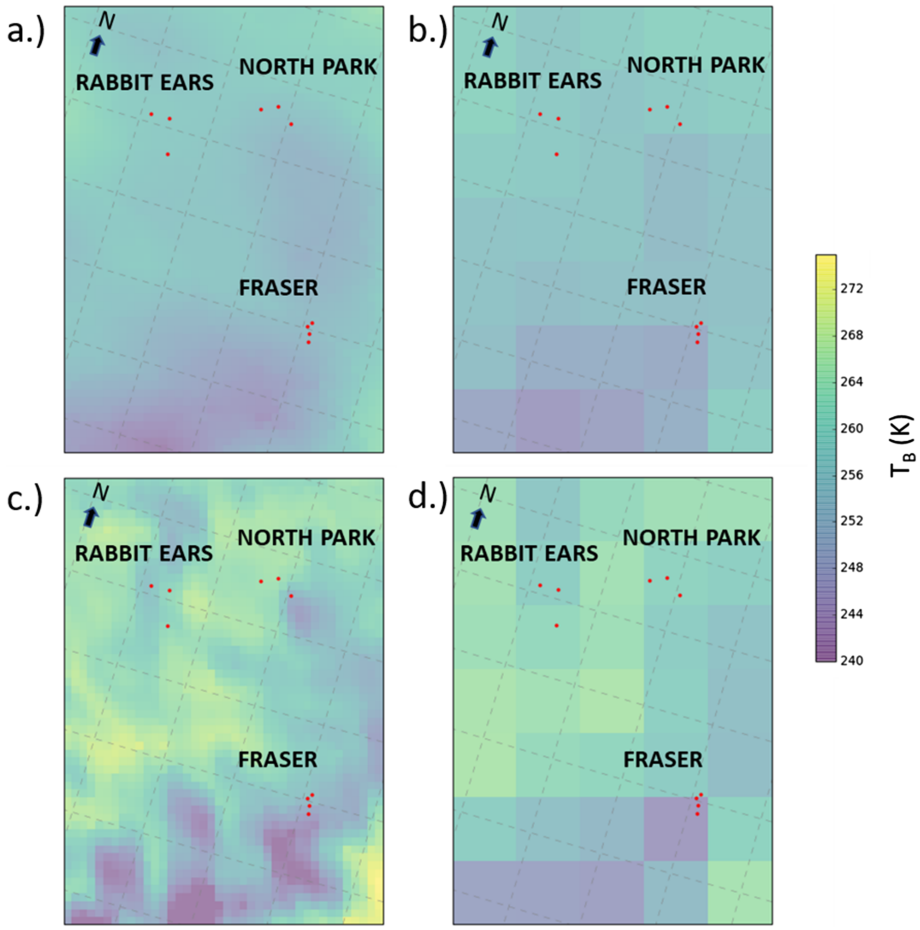

Figure 2. CETB 36/37 vertically-polarized brightness temperatures for February 14, 2003, subset to CLPX MSAs. rSIR (3-km pixels) at left and GRD (25-km pixels) at right. CLPX meteorological stations shown as red dots. SSM/I data shown in the top row and AMSR-E data are shown in the bottom row.

we could examine the number of detected and observed events as they vary with site characteristics such as elevation.

The algorithm performed most accurately at the Rabbit Ears sites (RS, RW, and RB), with true positive and true negative rates exceeding 76% for both sensors and resolutions. Error statistics were the poorest at the FHQ and FF stations with GRD data. True positive rates were 19% and 15% with AMSR-E and 25% and 33% with SSM/I. Melt detection with rSIR data at FHQ and FF performed significantly better, with true positive rates of 86% and 69% with AMSR-E, and 80% and 50% with SSM/I. See Supporting Information for full tables with all error statistics at each site. Note that the SSM/I statistics include only 6 or fewer melt events due to the high number of missed T_B observations at this latitude. Therefore, SSM/I was not able to detect any melt events during this period at FA, which is the highest elevation site (3585 m – meteorological station, 3457 m – average SIR pixel elevation) and experiences the coldest temperatures.

4.2. Melt Onset Date (MOD)

We examined the time series of snow depth and daily average air temperature from mid-winter through the snowmelt season at the CLPX stations and compared them with T_B and DAV at each pixel resolution. This allows us to examine the differences in the microwave signal at each resolution and how they compare with ground observations. Figure 4 shows time series for the FHQ site for rSIR and GRD data for both the AMSR-E and SSM/I sensors.

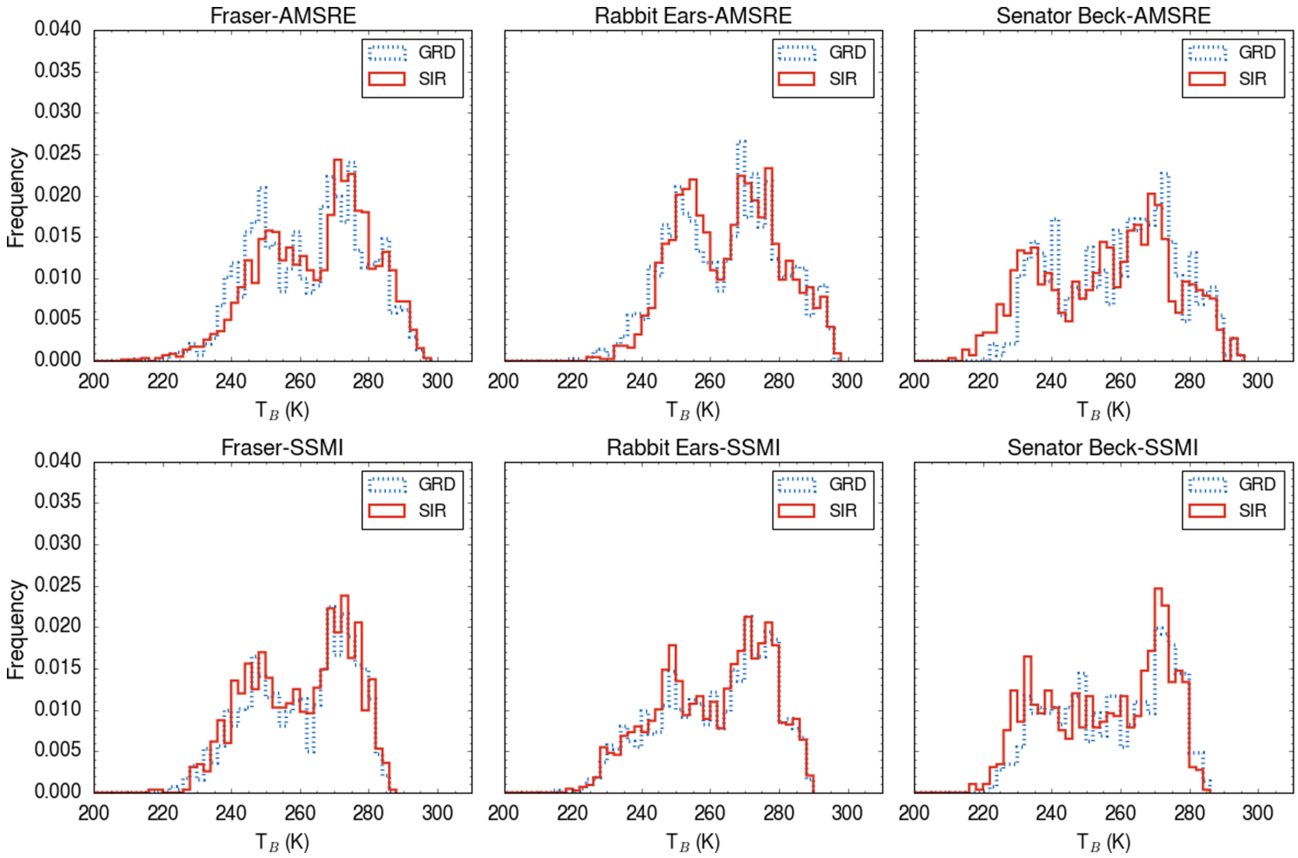

Figure 3. Histograms of T_B (x-axis) Fraser, Rabbit Ears, and Senator Beck for melt threshold determination. Histograms plot the temporal distribution of T_B data from all rSIR pixels and GRD pixel(s) that enclose each site. AMSR-E data plotted in the top row; SSM/I data in the bottom row.

MOD is defined when both T_B and DAV thresholds are exceeded a specified number of times within a specified time window. For AMSR-E, the MOD algorithm is defined as five DAV and T_B threshold exceedances in a seven-day window, with a DAV threshold of 18 K and a T_B threshold of 250 K. For SSM/I, we use a slightly modified algorithm with MOD estimated as the date with three T_B and DAV exceedances in a five-day window, with a DAV threshold of 10 K and a TB threshold of 247 K. Higher thresholds are needed for AMSR-E since the time series of T_B and DAV shows a higher average than SSM/I. SSM/I uses a smaller melt window (3/5 vs. 5/7) because the SSMI sensor has more missed measurements at this latitude than AMSRE, and a 5/7 exceedance algorithm missed the ablation periods. We used the same T_B thresholds for both winter melt events and MOD. The thresholds used for the MOD algorithm were similar to thresholds used in northern Canada with legacy AMSR-E data (Apgar et al., 2007). However, we used higher DAV thresholds for MOD detection than the previously determined winter melt event thresholds. Higher DAV thresholds are needed to detect seasonal MOD versus winter melt events since DAV increases with snow metamorphism later into the melt season.

All four of the estimated MODs coincided with ablation periods as observed from co-occurring snow depth and air temperature data at the nearest station. The rSIR data estimated an earlier MOD than GRD data for both sensors. For the higher-resolution rSIR data, the AMSR-E and SSM/I sensors showed MODs within 1 day of each other, on March 6 and March 7, respectively. The GRD datasets showed later MODs at April 9 and April 28 for AMSR-E and SSM/I, respectively. This earlier MOD estimated with the higher resolution datasets is important to note.

Table 1
Optimized TB and DAV thresholds yielding greatest accuracy for CLPX sites (FA, FS, RB, RW). Rates and number of winter melt events are shown. The test period was from January 1, 2003 to the date of peak snowpack at each site.

Sensor	AMSR-E		SSM/I	
T_B/DAV Thresholds	249 K/13 K (rSIR)	243 K/14 K (GRD)	247 K/10 K (rSIR)	247 K/10 K (GRD)
R_{TP} (TP)	86% (57)	83% (55)	90% (26)	91% (29)
R_{FN} (FN)	14% (9)	17% (11)	10% (3)	9% (3)
R_{TN} (TN)	81% (201)	75% (187)	87% (118)	89% (155)
R_{FP} (FP)	19% (48)	25% (62)	13% (17)	11% (20)

Table 2
Validated TB and DAV thresholds at remaining CLPX sites (FF, FHQ, RS). Rates and number of winter melt events are shown. The test period was from January 1, 2003 to the date of peak snowpack at each site.

Sensor	AMSR-E		SSM/I	
T_B/DAV Thresholds	249 K/13 K (rSIR)	243 K/14 K (GRD)	247 K/10 K (rSIR)	247 K/10 K (GRD)
R_{TP} (TP)	78% (46)	46% (27)	83% (19)	65% (13)
R_{FN} (FN)	22% (13)	54% (32)	17% (4)	35% (7)
R_{TN} (TN)	83% (118)	86% (123)	94% (104)	92% (71)
R_{FP} (FP)	17% (25)	14% (20)	6% (7)	8% (6)

The FHQ station sits at 2760 m, and its average rSIR pixel elevation is 2948 m. However, it is located in a low-lying area of a high-relief GRD pixel, and its average GRD pixel elevation is 3356 m. A comparison of DAV time series at for each pixel shows higher DAV throughout the winter for the rSIR versus the GRD pixel.

We expanded this MOD analysis with the same algorithm to Senator Beck Basin in Figure 6 and compared the concurrent CETB and snowpack data to measured streamflow. Snow depth, as measured at each station, and discharge at the Senator Beck stream gage are shown for water years 2006-2008. The rising limb of the streamflow hydrograph closely follows the algorithm-estimated MODs for both sensors and resolutions. MODs also coincide with periods of ablation from observed ground data. We applied the same thresholds

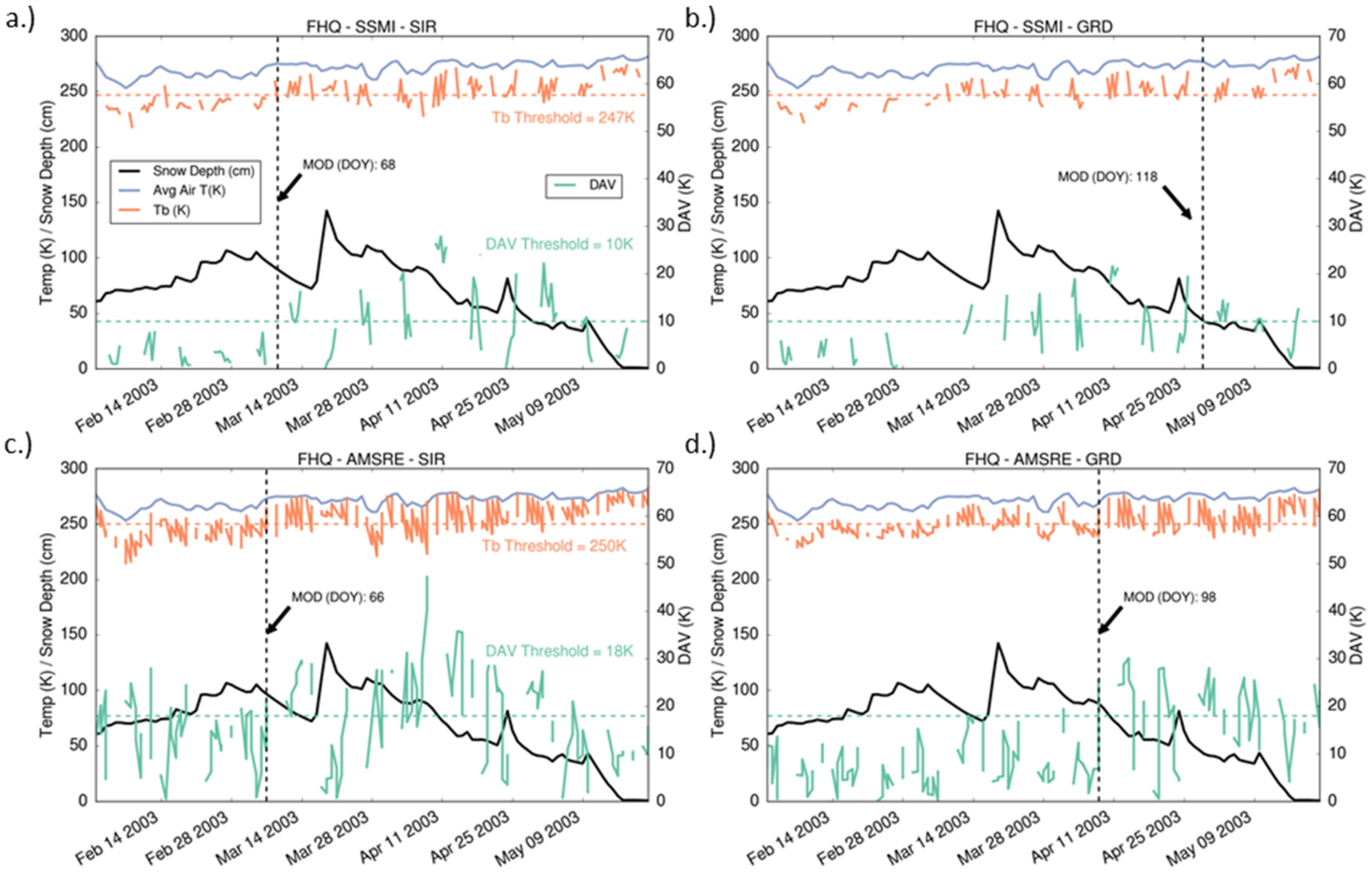

Figure 4. Fraser Headquarters (FHQ) time series of 36V T_B (green), DAV (red), Average Air Temperature (K) (blue), and Snow Depth (m) (black) for AMSR-E and SSM/I sensors. The top panels (a-b.) show the data for the SSM/I sensor and the bottom panels (c-d.) show AMSR-E. rSIR shown on the left panels and GRD shown on the right. Algorithm calculated melt onset date (MOD) listed as day of year (DOY) in vertical black lines. Horizontal dashed lines indicate DAV (green) and T_B (red) thresholds used for the MOD algorithm.

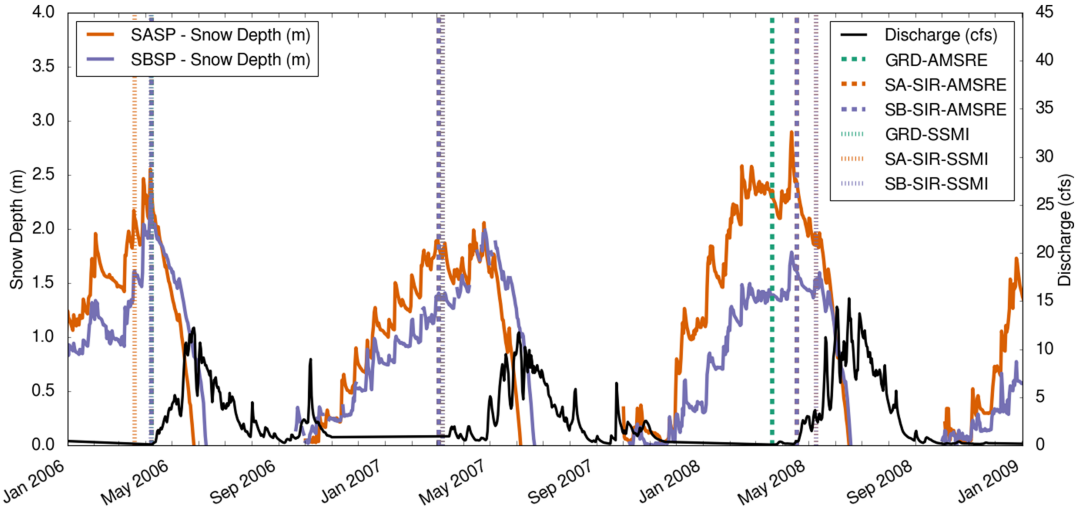

Figure 5. Time series of snow depth (solid blue lines) at Senator Beck Basin sites (Swamp Angel Study Plot – SASP) and Senator Beck Study Plot (SBSP) and stream discharge at Senator Beck Stream Gage (solid black line). Algorithm-calculated MODs with rSIR and GRD datasets for both sites shown as vertical lines.

used in Figure 5, along with the 5 out of 7 day exceedance MOD algorithm for AMSR-E and the 3 out of 5 day exceedance algorithm for SSM/I. The stations are located in the same catchment and adjacent rSIR pixels. Both stations are located in the same GRD pixel, so there is only one algorithm-estimated MOD. Note that a MOD with GRD data for SSM/I was not detected for water year 2008 because T_B and DAV thresholds for the specified window were never exceeded. This is likely due to the high frequency of missed measurements.

5. Discussion

Overall, the higher-resolution rSIR product was able to detect melt events at a higher rate of accuracy than the coarser-resolution GRD dataset. Melt detection performed better for sites where the rSIR pixel had a substantially different average elevation than the coarser GRD pixel containing the rSIR pixel. For the AMSR-E sensor, rSIR observations correctly detected 18 of 21 melt events at Fraser Headquarters (FHQ), while the GRD dataset detected only 4 of the 21 melt events during 2003 melt season. The FHQ station is located at 2760 m, its average rSIR pixel elevation is 2948 m, and its GRD pixel elevation is 3356 m. Since the rSIR pixel is more representative of the elevation at the station, it is possible that the higher resolution and site specific data are more representative than the GRD pixel. Furthermore, melt detection accuracy with AMSR-E at the Fraser Fool Creek (FF) station was also poor with the GRD product, where only 2 of 13 melt events were detected, while rSIR thresholds were able to detect 9 of these events. The FF station sits at 3100 m, its rSIR average pixel elevation is 2994 m, and it is located in the same GRD pixel as FHQ with an average pixel elevation of 3356 m. The Rabbit Ears site also showed that stations with low variation between station elevation, rSIR pixel elevation, and GRD pixel elevation showed similarly accurate melt detection rates. The Rabbit Ears Walton Creek (RW) site is located at 2950 m, its rSIR pixel elevation is 2953 m, and the GRD pixel elevation is 2772 m. For the RW site, the rSIR dataset detected 21 of 23 melt events, and the GRD dataset detected 19 of 23 melt events.

In addition to elevation data, land cover datasets could be incorporated to quantify the impacts of vegetation density and vegetation type on melt detection algorithm performance. Vegetation cover can attenuate the microwave signal and impact SWE algorithms (Kelly, 2009). Some preliminary analysis with land cover was conducted, but no patterns in melt detection were observed with respect to forest density. Land cover classifications for each EASE-Grid 2.0 pixel were examined in a product derived from the Boston University MODIS/Terra Land Cover Data product (Brodzik & Knowles, 2011). For the CLPX study area, average density of evergreen needleleaf forest ranged from 3% to 57% for GRD pixels, and from 0% to 100% for rSIR pixels. The presence of small amounts of moisture in the snowpack cause a large change in the microwave signal, so forest/non-forest land cover is thought to be a secondary feature in the DAV/T_B

variations during snowmelt. Future efforts will use land cover to identify the component of the microwave signal contributed by snow-covered forest.

The seasonal melt onset dates estimated by the DAV MOD algorithm were also consistent with site elevation. For the rSIR pixels, the 2003 MODs were later at higher elevations (March 6 at FS, March 7 at FHQ, April 6 at FF, and April 7 at FA). The MOD for the GRD pixel was April 8. Note that a "true" seasonal melt onset date is difficult to estimate in a mid-latitude environment like this since intermittent periods of melt and accumulation occur throughout January into May. However, the MOD estimated by the algorithm with rSIR pixels is detecting the beginning of a real period of ablation, but additional snow accumulation occurred after this MOD in some instances. Therefore, future studies could look to define more robust MOD thresholds by validating with better "true" MOD metrics.

Validating any satellite-derived dataset's ability to capture snowpack dynamics, and melt in particular, is dependent on the availability of in situ data to detect the snowpack evolution and melt events. It is also highly dependent on melt event definition. AMSR-E and SSM/I are able to detect snowmelt due to the difference in emissivity between frozen and liquid water states. In this case, a snowmelt event is the transition of water from frozen to liquid in the upper layers of the snowpack, which may or may not refreeze within the snowpack. This early near surface melt is important for remote sensing practitioners because surface wetness in the snow decreases the ability to use microwave approaches for measuring snow water equivalent, can impact snow structure such as developing snow crusts and layers, and may be of interest as winter characteristics change. This is compared to the definition used by water resource managers, which is the meltwater that leaves the snowpack to either infiltrate to groundwater or runoff into streams. Consequently, the traditional snowpack observations – depth and SWE – are useful for quantifying snowmelt for water resources, but insufficient for optimal calibration and validation of satellite-derived datasets. Ideally, snow wetness observations would be used, but this data is difficult and expensive to collect. The melt definition used here therefore represents a compromise due to data availability. The conditions, decreasing depth and air temperature above freezing, are necessary but insufficient conditions for snowmelt. As such, the method may lead to overdetection of melt events, particularly during mid-winter when incoming radiation is lower. Comparison with melt detection using SWE and air temperature at a nearby SNOTEL site resulted in the same melt events (See Supporting Information), with four melt events detected using depth that were not detected using SWE in mid-March and early-April. However, it is also possible that using a decrease in SWE as an indicator of melt might not detect small amounts of liquid water in the snow surface during intermittent subdaily melt, where the passive microwave sensor could detect this state change in the snow surface.

In this study, the DAV method for snowmelt is difficult to use with very shallow snowpacks because it is difficult to discern real melt events from diurnal air temperature swings and/or soil freeze/thaw. However, when snowpacks are shallow and intermittent, then snowmelt is also a less important component of the hydrologic cycle. We excluded North Park sites from the melt detection analysis for this reason. These sites showed a high winter DAV signal, which could be due to bare soil freeze-thaw cycles occurring throughout the winter (Matzler, 1994). Observed DAV at North Park sites was higher than at Fraser and Rabbit Ears. For the Fraser GRD pixel, the average January-February DAV for 2003 was 5.5 K, while the North Park GRD pixel showed an average DAV of 15K. North Park has markedly different site characteristics than Rabbit Ears and Fraser. It is lower elevation, lower relief, and has minimal tree cover. North Park also contains a higher percentage of wetlands and ponds than the other sites. The distinct DAV signal and unique site characteristics raise further research questions related to CETB and land cover. It is possible that a soil or surface water freeze-thaw signal is present in the CETB data. There has been some work on detecting soil freeze-thaw with passive microwaves (Kim et al., 2011; Matzler, 1994; Wegmüller, 1990; Zhang, 2003; Zhao et al., 2011; Zuerndorfer et al., 1990), but soil freeze-thaw was outside the scope of this study. CETB data could be studied for this application in the future.

There are several limitations to the CETB data, most of which are general limitations in the use of satellite-based passive microwave remote sensing. The occurrence of missed measurements in mid-latitude areas can be significant, with over 20% data gaps in Colorado for AMSR-E in a given year. SSM/I, with a narrower swath width, yielded even more missed measurements, with up to 40% missed at this latitude. This will cause the true number of melt events to be underestimated and increase the uncertainty of melt onset dates.

Missed measurements may cause a later MOD to be estimated than what might be true on the ground. This issue decreases at higher latitudes.

The T_B and DAV thresholds determined in our study provided reasonable snowmelt detection results for these select sites in Colorado in terms of winter melt events and seasonal melt onset dates when compared to concurrent meteorological ground data. They are similar to, but not identical to, melt thresholds from other regions and studies. However, it cannot be assumed that these thresholds will work in other regions and snow classes. Further work is needed to test these algorithms in other areas to determine if thresholds should be changed regionally. These CLPX sites are in close proximity to one another, but they do have some variation in land cover type and physiographic regime. The constant thresholds determined in this study worked for each of the sites, so it is possible that thresholds will not vary greatly with region or snow class. The CLPX data also only covers one snow season: further studies should incorporate more ground stations with more years of available data to develop greater confidence in the T_B and DAV thresholds.

6. Conclusions

The brightness temperature signal from the enhanced-resolution CETB product is more sensitive to hydrologic and snowpack processes than lower-resolution passive microwave products in a mountainous region of Colorado. This enabled the detection of melt events preceding the ablation season, which impact snowpack stratigraphy and metamorphism. Across all sites examined, time series show an increase in the magnitude of DAV during the snowmelt season, with the DAV decreasing during snowpack saturation and snow-off conditions. During times with snow cover, high DAV days coincide with days of air temperature >0°C from ground-based measurements. A DAV melt onset date algorithm was able to detect periods of snow ablation as observed from ground data, with higher resolution brightness temperature data detecting melt onset more accurately in high-relief terrain. The enhanced spatial resolution allows for improved detection of snow melt variability in heterogeneous terrain. This study raises numerous questions for future work. The CETB product should be tested in a wider range of environments over a larger time period to quantify its performance in different regions and snow classifications. Other snowmelt algorithms, such as the cross-polarization gradient ratio (XPGR), and additional passive microwave sensors, such as the Scanning Multichannel Microwave Radiometer (SMMR) and the series of Special Sensor Microwave Imager/Sounder (SSMIS), should be incorporated. The CETB product shows promise for snowmelt applications, and may also improve results of other passive microwave algorithms, including snow water equivalent estimates and the detection of soil freeze-thaw.

Acknowledgements and Data Availability

We would like to extend our thanks to our data providers: the National Snow and Ice Data Center (NSIDC) Distributed Active Archive Center (DAAC) for CLPX and CETB data, and the Center for Snow and Avalanche Studies (CSAS) for Senator Beck Basin data. Additional thanks to Kelly Elder for assistance with CLPX data, and Katrina Gelwick for GIS assistance and three anonymous reviewers for their insightful comments. Funding was provided by US Army Cold Regions Research and Engineering Laboratory, Science and Technology Corporation, Lehigh University P.C. Rossin College of Engineering and Applied Science, and Lehigh University College of Arts and Sciences. The CETB data are available for download at https://nsidc.org/data/nsidc-0630, the CLPX data are available at https://nsidc.org/data/nsidc-0172, and the CSAS data at https://snowstudies.org/archived-data/. The code used to create the figures is at https://gitlab.com/tjtroy/cetb_clpx.

References

Apgar, J. D., Ramage, J. M., Mckenney, R. A., & Maltais, P. (2007). AMSR-E algorithm for snowmelt onset detection in sub-arctic heterogeneous terrain. *Hydrological Processes*, *21*, 1587–1596. https://doi.org/10.1002/hyp.6721

Bales, R. C., Molotch, N. P., Painter, T. H., Dettinger, M. D., Rice, R., & Dozier, J. (2006). Mountain hydrology of the western United States. *Water Resources Research*, *42*, W08432. https://doi.org/10.1029/2005WR004387

Barnett, T. P., Adam, J. C., & Lettenmaier, D. P. (2005). Potential impacts of a warming climate on water availability in snow-dominated regions. *Nature*, *438*(7066), 303–309. https://doi.org/10.1038/nature04141

Brodzik, M. J., & Knowles, K. (2011). EASE-Grid 2.0 Land Cover Classifications Derived from Boston University MODIS/Terra Land Cover Data, Version 1. *NASA National Snow and Ice Data Center Distributed Active Archive Center*. https://doi.org/https://doi.org/10.5067/XR8523MC24TB

Brodzik, M. J., Long, D. G., Hardman, M. A., Paget, A., & Armstrong, R. L. (2018). MEaSUREs Calibrated Enhanced-Resolution Passive Microwave Daily EASE-Grid 2.0 Brightness Temperature ESDR, Version 1.3. NASA National Snow and Ice Data Center Distributed Active Archive Center. Retrieved from https://doi.org/10.5067/MEASURES/CRYOSPHERE/NSIDC-0630.001

Burke, H. H. K., Bowley, C. J., & Barnes, J. C. (1984). Determination of snowpack properties from satellite passive microwave measurements. *Remote Sensing of Environment*, *15*(1), 1–20. https://doi.org/10.1016/0034-4257(84)90048-8

Chang, A. T. C., Gloersen, P., Schmugge, T., Wilheit, T. T., & Zwally, H. J. (1976). Microwave emission from snow and glacier ice. *Journal of Glaciology*, *16*(74), 23–39. https://doi.org/10.1017/S0022143000031415

Cline, D., Elder, K., Davis, R., Armstrong, R. L., & Liston, G. E. (2001). NASA Cold Land Processes Field Experiment Plan 2001-2004. Retrieved from https://www.nohrsc.noaa.gov/~cline/clpx.html

Elder, K., & Goodbody, A. (2004). CLPX-Ground: ISA Main Meteorological Data, Version 1|National Snow and Ice Data Center. Retrieved October 31, 2018, from https://nsidc.org/data/NSIDC-0172/versions/1

Elder, K., Goodbody, A., Cline, D., Houser, P., Liston, G. E., Mahrt, L., & Rutter, N. (2009). NASA Cold Land Processes Experiment (CLPX 2002/03): Ground-Based and Near-Surface Meteorological Observations. *Journal of Hydrometeorology*, *10*(1), 330–337. https://doi.org/10.1175/2008JHM878.1

Foster, J. L., Hall, D. K., Chang, A. T. C., & Rango, A. (1984). An Overview of Passive Microwave Snow Research and Results. *Reviews of Geophysics*, *22*(2), 195–208.

Foster, J. L., Hall, D. K., Eylander, J. B., Riggs, G. A., Nghiem, S. V., Tedesco, M., et al. (2011). A blended global snow product using visible, passive microwave and scatterometer satellite data. *International Journal of Remote Sensing*, *32*(5), 1371–1395. https://doi.org/10.1080/01431160903548013

Kelly, R. (2009). The AMSR-E Snow Depth Algorithm: Description and Initial Results. *Journal of the Remote Sensing Society of Japan*, *29*(1), 307–317. https://doi.org/10.11440/rssj.29.307

Kim, Y., Kimball, J. S., McDonald, K. C., & Glassy, J. (2011). Developing a Global Data Record of Daily Landscape Freeze/Thaw Status Using Satellite Passive Microwave Remote Sensing. *IEEE Transactions on Geoscience and Remote Sensing*, *49*(3), 949–960. https://doi.org/10.1109/TGRS.2010.2070515

Kopczynski, S. E., Ramage, J. M., Lawson, D., Goetz, S., Evenson, E., Denner, J., & Larson, G. (2008). Passive microwave (SSM/I) satellite predictions of valley glacier hydrology, Matanuska Glacier, Alaska. *Geophysical Research Letters*, *35*, L16502. https://doi.org/10.1029/2008GL034615

Landry, C. C., Buck, K. A., Raleigh, M. S., & Clark, M. P. (2014). Mountain system monitoring at Senator Beck Basin, San Juan Mountains, Colorado: A new integrative data source to develop and evaluate models of snow and hydrologic processes. *Water Resources Research*, *50*, 1773–1788. https://doi.org/10.1002/2013WR013711

Li, D., Durand, M., & Margulis, S. A. (2012). Potential for hydrologic characterization of deep mountain snowpack via passive microwave remote sensing in the Kern River basin, Sierra Nevada, USA. *Remote Sensing of Environment*, *125*, 34–48. https://doi.org/10.1016/j.rse.2012.06.027

Long, D. G., & Brodzik, M. J. (2016). Optimum Image Formation for Spaceborne Microwave Radiometer Products. *IEEE Transactions on Geoscience and Remote Sensing*, *54*(5), 2763–2779. https://doi.org/10.1109/TGRS.2015.2505677

Mätzler, C. (1987). Applications of the interaction of microwaves with the natural snow cover. *Remote Sensing Reviews*, *2*(2), 259–387. https://doi.org/10.1080/02757258709532086

Matzler, C. (1994). Passive Microwave Signatures of Landscapes in Winter. *Meteorological Atmospheric Physics*, *54*, 241–260. https://doi.org/10.1016/j.neuroimage.2008.09.022

McCabe, G. J., & Clark, M. P. (2005). Trends and Variability in Snowmelt Runoff in the Western United States. *Journal of Hydrometeorology*, *6*, 476–482.

Monahan, P. A., & Ramage, J. M. (2010). AMSR-E melt patterns on the Southern Patagonia Icefield. *Journal of Glaciology*, *56*(198), 699–708. https://doi.org/10.3189/002214310793146197

Ramage, J. M., & Isacks, B. L. (2002). Determination of melt-onset and refreeze timing on southeast Alaskan icefields using SSM/I diurnal amplitude variations. *Annals of Glaciology*, *34*, 391–398. https://doi.org/doi:10.3189/172756402781817761

Ramage, J. M., McKenney, R. A., Thorson, B., Maltais, P., & Kopczynski, S. E. (2006). Relationship between passive microwave-derived snowmelt and surface-measured discharge, Wheaton River, Yukon Territory, Canada. *Hydrological Processes*, *20*(4), 689–704. https://doi.org/10.1002/hyp.6133

Regonda, S. K., Rajagopalan, B., Clark, M. P., & Pitlick, J. (2005). Seasonal cycle shifts in hydroclimatology over the western United States. *Journal of Climate*, *18*(2), 372–384. https://doi.org/10.1175/JCLI-3272.1

Sapiano, M. R. P., Berg, W. K., McKague, D. S., & Kummerow, C. D. (2013). Toward an intercalibrated fundamental climate data record of the SSM/I sensors. *IEEE Transactions on Geoscience and Remote Sensing*, *51*(3), 1492–1503. https://doi.org/10.1109/TGRS.2012.2206601

Semmens, K. A., Ramage, J. M., Apgar, J. D., Bennett, K. E., Liston, G. E., & Deeb, E. (2014). Passive Microwave Remote Sensing of Snowmelt and Melt-Refreeze Using Diurnal Amplitude Variations. *Remote Sensing of Environment*, 215–226). Retrieved from http://onlinelibrary.wiley.com/doi/10.1002/9781118872086.ch13/summary

Semmens, K. A., Ramage, J. M., Bartsch, A., & Liston, G. E. (2013). Early snowmelt events: Detection, distribution, and significance in a major sub-arctic watershed. *Environmental Research Letters*, *8*(1). https://doi.org/10.1088/1748-9326/8/1/014020

Serreze, M. C., Clark, M. P., Armstrong, R. L., Mcginnis, D. A., & Pulwarty, R. S. (1999). Characteristics of the western United States snowpack from snowpack telemetry (SNOTEL) data Program of Regional Integrated Assessments, Office of Global Programs, National Oceanic and Atmospheric Administration, Silver Spring, Maryland. *Water Resources Research*, *35*(7), 2145–2160. https://doi.org/10.1029/1999WR900090

Stewart, I. T. (2009). Changes in snowpack and snowmelt runoff for key mountain regions. *Hydrological Processes*, *23*, 78–94. https://doi.org/10.1002/hyp

Stewart, I. T., Cayan, D. R., & Dettinger, M. D. (2004). Changes toward Earlier Streamflow Timing across Western North America. *Journal of Climate*, *18*, 1136–1155. https://doi.org/10.1007/978-3-642-10248-6_1

Stiles, W. H. (1980). Microwave remote sensing of snowpacks. *Dissertation Abstracts International Part B: Science and Engineering[DISS. ABST. INT. PT. B.- SCI. & ENG.]*, *41*(5), 1980.

Sturdivant, E. J., Frey, K. E., & Urban, F. E. (2019). Snowmelt detection from QuikSCAT and ASCAT satellite radar scatterometer data across the Alaskan North Slope. *GIScience & Remote Sensing*, *56*(1), 87–108. https://doi.org/10.1080/15481603.2018.1493045

Tedesco, M. (2007). Snowmelt detection over the Greenland ice sheet from SSM/I brightness temperature daily variations. *Geophysical Research Letters*, *34*, L02504. https://doi.org/10.1029/2006GL028466

Tedesco, M., Abdalati, W., & Zwally, H. J. (2007). Persistent surface snowmelt over Antarctica (1987-2006) from 19.35 GHz brightness temperatures. *Geophysical Research Letters*, *34*, L18504. https://doi.org/10.1029/2007GL031199

Tedesco, M., Brodzik, M., Armstrong, R., Savoie, M., & Ramage, J. (2009). Pan arctic terrestrial snowmelt trends (1979 – 2008) from spaceborne passive microwave data and correlation with the. *Arctic Oscillation*, *36*, 1–6. https://doi.org/10.1029/2009GL039672

Tuttle, S. E., & Jacobs, J. M. (2019). Enhanced Identification of Snow Melt and Refreeze Events From Passive Microwave Brightness Temperature Using Air Temperature. *Water Resources Research*, *55*(4), 3248–3265. https://doi.org/10.1029/2018WR023995

USDA NRCS. (2019). Arapaho Ridge SNOTEL. Retrieved September 16, 2019, from https://wcc.sc.egov.usda.gov/nwcc/site?sitenum=1030

USGS. (2013). USGS NED 1/3 arc-second 2013 1 x 1 degree ArcGrid. Retrieved October 31, 2018, from https://www.sciencebase.gov/catalog/item/581d224ee4b08da350d547f7

Vuyovich, C., & Jacobs, J. M. (2011). Snowpack and runoff generation using AMSR-E passive microwave observations in the Upper Helmand Watershed, Afghanistan. *Remote Sensing of Environment*, *115*(12), 3313–3321. https://doi.org/10.1016/J.RSE.2011.07.014

Wegmüller, U. (1990). The effect of freezing and thawing on the microwave signatures of bare soil. *Remote Sensing of Environment*, *33*(2), 123–135. https://doi.org/10.1016/0034-4257(90)90038-N

Zhang, T. (2003). Investigation of the near-surface soil freeze-thaw cycle in the contiguous United States: Algorithm development and validation. *Journal of Geophysical Research*, *108*(D22), 8860. https://doi.org/10.1029/2003JD003530

Zhao, T., Zhang, L., Jiang, L., Zhao, S., Chai, L., & Jin, R. (2011). A new soil freeze/thaw discriminant algorithm using AMSR-E passive microwave imagery. *Hydrological Processes*, *25*(11), 1704–1716. https://doi.org/10.1002/hyp.7930

Zuerndorfer, B. W., England, A. W., Dobson, M. C., & Ulaby, F. T. (1990). Mapping freeze/thaw boundaries with SMMR data. *Agricultural and Forest Meteorology*, *52*(1–2), 199–225. https://doi.org/10.1016/0168-1923(90)90106-G